Seamount effects and shallow hydrothermal plumes in the Mariana Arc: impacts on chlorophyll concentrations and phytoplankton communities

Zoe Friedland

University of Washington, Seattle, WA

School of Oceanography

zoe@friedland.us

5 June 2026

Abstract

Seamount effects describe phenomena associated with bio-physical coupling at seamounts, often localized chlorophyll anomalies or shifts in community composition. Shallow seamount-associated hydrothermal plumes can also influence the euphotic zone, and metal requirements and toxicity thresholds vary across taxa. This study characterized the interactions between hydrography, chlorophyll, nutrients, hydrothermal plumes, and phytoplankton community composition at the deep chlorophyll maximum (DCM) across four seamounts (Ruby, Esmeralda, NW Rota-1, and Tracey) in the Mariana arc during a 10-day transect in late March 2026 aboard the *R/V* Thompson. Depth-integrated chlorophyll at Ruby was 300% higher than at all other locations (Tukey HSD, $p < 0.0005$) alongside faster outward-radiating currents, despite an absence of isopycnal doming or hydrothermal activity. Hydrothermal plumes were identified at NW Rota (400–450 m depth) through concurrent chemical and optical anomalies, including elevated dFe (5-17nM) and dMn (2nm) above background values (dFe: <2nm, dMn < 0.05nM). Very high dFe (15-35nM) was also measured at 200m at Esmeralda. $Si(OH)_4$ was significantly elevated at seamounts with hydrothermal plumes within the mixed layer, while NH_4 was elevated beneath it. Surface *Crocosphaera* biomass was higher at active than at inactive seamounts (Tukey HSD, $p = 0.035$). Microscopic identification of net tow samples at the DCM observed the same four most abundant taxa (Radiozoa, Bacillariophyceae, Dinophyceae, and Ciliophora) at all stations regardless of seamount proximity or plume influence (ANOSIM with Bray-Curtis dissimilarity R-statistic: 0.333, $p = 0.1431$). These findings indicate strong spatial patchiness in chlorophyll driven by the dynamic topography of the Mariana arc region, but no detectable restructuring of the dominant phytoplankton taxa at the DCM, establishing a baseline in the region for future work; these findings especially indicate a need to understand the synergistic

impacts of shallow plume Fe and $Si(OH)_4$ fertilization on silicious phytoplankton and the role of diazotrophs in a hydrothermal plume-influenced oligotrophic region.

Plain Language Summary

Seamounts are underwater mountains, many of them volcanically active, that can disrupt ocean currents and support unusually productive phytoplankton (or algal) communities in otherwise nutrient poor water, a so-called “seamount effect”. Hydrothermally active seamounts release plumes of metal-enriched waters, influencing the phytoplankton for which these metals are both essential nutrients and toxic at higher concentrations. However, the relative contributions of physical circulation effects and hydrothermal plumes in driving biological responses remain poorly understood. This study investigated the relationship between circulation changes, hydrothermal plumes, and phytoplankton at four Mariana arc seamounts. A 300% increase in chlorophyll was observed at Ruby seamount. Hydrothermal plumes were identified by their unique chemical and turbidity (or water cloudiness) signals at NW Rota-1 and Esmeralda seamounts. Near where plumes were identified, concentrations of iron, manganese, silica, and ammonium were also enhanced. Phytoplankton cells from net tows at seamounts were counted and identified to determine if there were changes in communities due to hydrothermal plumes or nutrients, but no changes were detectable based on the sample size and sampling methods. This study measured a seamount effect at Ruby seamount compared to other seamounts, but no seamount effects at seamount summits relative to their flanks. Additionally, while the plume at Esmeralda was likely shallow enough to influence phytoplankton, no effects on the community structure of different types of phytoplankton were detected.

1 Introduction

As the warmest pool of water on the planet, the Western Warm Pacific Pool is a unique region characterized by intensely stratified and oligotrophic waters, and its contribution to air temperature and moisture has an outsized influence on global climate (Jin et al. 2024). The Mariana Arc system's numerous seamounts are located within it, of which many contain active hydrothermal plumes (Baker et al. 2008). Previous research has described a "seamount effect", or the observation that seamounts can stimulate primary productivity and changes in community composition, but the underlying mechanisms and the reason behind inconsistent observations of this effect remain poorly understood. Both seamount-associated impacts on physical circulation and seamount-associated hydrothermal plumes may be involved in stimulating or altering biological processes. Thus, there are potential implications for long-term climate warming and interannual ENSO variability on biological productivity in this uniquely oligotrophic region, and downstream implications for carbon export in the region due to shifts in the balance of small, surface-water occupying phytoplankton relying on regenerated nutrients and larger taxa that are more macronutrient limited (Eppley & Peterson 1979).

As a physical barrier in the water column, seamounts have been observed to impact water circulation and drive upwelling, specifically driving vertical circulation, internal tides, turbulence, and Taylor columns, also known as Taylor cones. This is generally observed through the uplift of nutrient isoclines (isopycnal doming) around seamount summits (Clark et al. 2010). Such impacts are thought to be responsible for the "seamount effect" of shallower seamounts, as they are close enough to the surface to push nutrients into the euphotic zone (<200m). A Taylor cone forms in relatively barotropic fluid (i.e., the density gradient is only a function of the pressure gradient) and creates an anticyclonic flow in the Northern Hemisphere around a seamount, but the effect is decreased if there is too much stratification. However, more recent

92 work has found that very deep seamounts can also exhibit a seamount effect (Dai et al. 2022). In
93 this case, involved physical ocean processes are hypothesized to be primarily the result of
94 internal tides, rather than Taylor cones (Dai et al. 2022). Mesoscale eddies can also alter the
95 seamount effect, shifting the dominant communities between nano- and pico-plankton, according
96 to a study over a seamount in Madagascar where samples were taken inside of a dipole eddy
97 (Rocke et al. 2020).

98 Where such mechanistic explanations are inconsistently observed or difficult to attribute
99 to real data due to variability between seamounts, seasonal changes to hydrography, and
100 sampling resolution limitations, they are well-supported by biogeochemical modeling. A
101 modified version of the Nutrient-Phytoplankton-Zooplankton-Detritus (NPDZ) model by
102 Oschlies and Garcon 1999 demonstrated that the highest rates of primary productivity are
103 stimulated by upwelling in combination with horizontal mixing, and when upwelling occurs in
104 multiple localized instances rather than within one large water mass (Martin et al. 2001). Arc
105 seamounts are thus environments where one might expect to observe high increases in primary
106 productivity. Further observations of actual productivity at seamounts are crucial to improve the
107 accuracy of these models.

108 Lastly, the biological impact of physical circulation around seamounts tends to be
109 asymmetric, with observations of increased productivity occurring downstream of the
110 seamount. Multiple transects at the nearby Kocebu seamount in the Western Warm Pacific
111 demonstrated that downstream localization of effects is patchy, however, and does not only
112 reflect overall changes in productivity but spatially distributed blooms of different taxa (Dai et
113 al. 2020, Dai et al. 2022).

Seamount associated increases in chlorophyll-a as a proxy for biomass are generally two-to-fourfold that of off-seamount samples according to previous results on the Kocebu and Cobb seamounts (Dai et al. 2020, Dai et al. 2022, Comeau et al. 1995). Size-fractionated studies on chl *a* reveal that that picoplankton (<2 μm) consistently dominate on and off seamounts, contributing ~85% of chl *a* at these seamounts (Dai et al. 2020, Dai et al. 2022). At the Kocebu seamount (located at 17º N 153º E), phytoplankton taxa were dominated by cyanobacteria including prochlorophytes, with a small presence of dinoflagellates and diatoms peaking at ~100m, and increasing haptophytes, cryptophytes, and chrysophytes with greater depth down to 200m. In a 2023 survey of phytoplankton diversity across the Equatorial Pacific, diversity remained consistent across the 141ºE transect within the latitudes between 10-20º (Yan et al. 2023). Here, it was around 2.5-3, lower than the peak diversities (upwards of 3.5) measured along the Southern Equatorial Current, but still higher compared to the values measured only a few degrees beyond 20ºN, where diversity rapidly dropped off (0.5 to 1) into the lowest values recorded in the entire study (Yan et al. 2023). These dramatic changes in phytoplankton diversity along the 141ºE longitude indicate the need to further resolve the dynamics of biological communities and the role of the seamounts in the area.

The other potential mechanism driving the seamount effect describes not only the general effect of seamount-driven upwelling but the allochthonous nutrient input from hydrothermal plumes. Hydrothermal plumes are chemically distinct from normal seawater and contain uniquely high levels of trace metals not otherwise found in the ocean (Twining & Baines 2013). The redox states of these metals are complex and variable, but generally, vent systems are highly reducing environments that release hot plumes of dissolved metals and hydrogen sulfide. These plumes rise quickly before undergoing lateral mixing at depths determined by the rate of heat

loss and density equilibration (Twining & Baines 2013). Oxidation necessarily occurs throughout this process, resulting in some metal precipitation and settling, while others remain bioavailable through both inorganic and organic complexation and particle adsorption (Kleint et al. 2022, Sunda 2012). In the deep vent systems of spreading ridges, this makes it difficult for vent input to impact the euphotic zone, though metals may still travel thousands of kilometers laterally (Fitzsimmons et al. 2014). The shallow height of seamounts, on the other hand, makes euphotic-layer interactions more relevant, which may in turn impact lateral transport due to ligand-binding, biotic particle adsorption, and intracellular stoichiometry altering metal ratios (Sunda 2012, Kleint et al. 2022).

Trace metals are not only a passive constituent of biological activity but essential to many vital phytoplankton processes, while some are toxic above threshold levels (notably Cd and Cu) (Twining & Baines 2013). Specific concentrations can differ among taxa even more than they shift with changing environmental conditions (Twining & Baines 2013). Different taxa also have different abilities to respond effectively to pulsed inputs by storing extra metals for later use or by down-regulating uptake receptors to protect against toxicity (Twining & Baines 2013). Additionally, multiple metals may compete for the same receptors, and deficiencies in one metal can increase cellular demand for another (Twining & Baines 2013). This complexity presents a cascade of possibilities for plume waters to shift the relative abundances of phytoplankton taxa near a seamount. Phytoplankton possess an extremely diverse set of requirements, sensitivities, and adaptations to regulate internal levels against external concentrations, with differences occurring on multiple levels of evolutionary lineage (Sunda 2012, Twining & Baines 2013). This diversity makes predictions on community assemblage responses to environmental shifts difficult.

The proximity of shallow seamount-associated hydrothermal vents to the euphotic zone is not the only mechanism influencing their distribution, because physical mixing induced by a seamount does not differentiate between macronutrients and exotic plume constituents. Even in the absence of plumes, seamounts are hotspots for the formation of cobalt-rich ferromanganese crusts along their slopes, and these represent an additional seamount-associated source of ambient trace metals (Liao et al. 2011). In a study on the M4 seamount, this was discussed as the likely mechanism for their finding of small seamount-associated impacts to the vertical distribution of trace metals—small, because the values were within an order of magnitude of background reference levels for each metal in ambient seawater (Ma et al. 2023). This finding verifies the capacity of this research to distinguish from crust-derived benthic metal fluxes and plume waters on the basis of concentration level without using isotropic tracers, because the concentrations of metals sampled from plumes are consistently higher than at sampling sites where plumes are not presence. It also suggests that even small increases in trace metals may have biological impacts, due to the notable correlations between specific trace metals and biogenic macronutrients or chl *a* (Ma et al. 2023). Phytoplankton not only respond to concentrations of metal in the water through tightly regulated uptake mechanisms, but influence it in turn as they die, transporting metals back to the seafloor in the ratio that it was present in their cells. That trace metals correlate with biological indicators even at sub-plume concentrations underscores how much stronger those relationships may be near active plumes.

This study hypothesizes that seamount-induced upwelling will produce two-to-fourfold increases in biomass, while shifts to the relative abundance of phytoplankton taxa will occur only over seamounts with active hydrothermal plumes. Advances in ocean technology have only recently allowed for high-resolution seafloor mapping and detection of plumes, so their influence

on the biology of the euphotic zone remains understudied. Improving our understanding of the bio-chemical coupling of plumes will provide basis and direction for future work considering these technologies, as well as increase the accuracy of biogeochemical models.

2 Methods

2.1 Study area

The region of study included seamounts Ruby (15.62°N, 145.57°E), Esmeralda (14.97°N, 145.29°E), NW Rota-1 (14.62°N, 144.78°E), and Tracey (13.63°N, 144.46°E) and two offshore stations near the Mariana trench (14.35°N, 148.5°E; 14.91°N, 146.59°E). Cruise duration was 10 days between 22 March and 1 April 2026.

GEBCO 2025 15-arc second bathymetry data was used to create maps of cruise stations in Python and assess the hydrographic characteristics of seamounts in the region.

2.2 CTD-Rosette sensor suite and water column analysis

Water column sampling was conducted using a Sea-Bird SBE 911plus CTD rosette system (Sea-Bird Scientific) fitted with 24 10-L Niskin bottles. The sensor suite included a Sea-Bird SBE 43 Dissolved Oxygen Sensor, a WET Labs ECO-AFL/FL Fluorometer, a WET Labs C-Star Transmissometer and a Biospherical QSP-2300 photosynthetically active radiation (PAR) sensor (Seabird Scientific). A homemade oxidation, reduction potential (ORP) sensor was also attached; this sensor detects reducing fluids indicative of hydrothermal fluids and reports Eh values as dimensionless units.

SeaSoft V2 via SeaBird was used to process raw files for CTD casts into netCDF. The mixed-layer depth (MLD) was detected at the depth at which a change in temperature was

recorded greater than 0.2°C with respect to a reference temperature as the mean temperature from 0 to 15m depth.

The deep chlorophyll maximum (DCM) was defined as the depth of the deep fluorescence maximum (DFM), as recorded by the CTD fluorometer on the downcast. The full band of the DCM was defined as 1m above the MLD (to better control for differences in stratification intensity) to 50m beneath the DCM, and this was the region over which depth-integrated fluorescence was estimated using numpy.trapezoid.

The DCM offset from the MLD was defined as Z_{DCM}-Z_{MLD}; positive values indicate the depth of the DCM was beneath the MLD at that station.

2.3 Nutrients

Seawater was collected from Niskin bottles through a triple-rinsed 0.2 µm syringe filter into 60mL bottles and stored at -20° for offshore analysis. Nutrients were analyzed with a Seal Analytical AA3 autoanalyzer by the UW Marine Chemistry Laboratory following Gordon et al. (1993) WOCE protocol (Gordon et. al 1993).

2.4 Chlorophyll *a*

Seawater for chlorophyll *a* analysis was collected from Niskin bottles into 1L bottles and extracted in 500ml replicates. These samples were vacuum-filtered through 0.7 µm glass-fiber filters. Chlorophyll was extracted from filters using the acetone method at -20°C for 24 hours, following Strickland & Parsons 1972, and fluorescence measured on a TD-700 fluorometer (Turner Designs) (Strickland & Parsons 1972).

2.5 Trace metals

Teflon-coated internal springs were used on even Niskin bottles for trace metal sample collection and all trace metal samples were filtered immediately through a a 0.2 μm capsule filter (Acropak 200, Pall Corporation).

At select stations seawater was collected at 15m using polyethylene tubing lowered on a braided nylon line connected to a Teflon diaphragm pump (Walden Incorporated), avoiding trace metal contamination. Filtered samples were collected through a 0.2 μm capsule filter (Acropak 200, Pall Corporation).

All trace metal samples were acidified to pH 1.8 (Optima HCl, Fisher Scientific) within one week of collection. Samples where the estimated dFe (dissolved Fe) concentration was likely to exceed 20 nM (i.e., suspected plume samples based on ORP and turbidity readings during CTD casts) were pre-treated by adding 167 μL of the acidified sample to mL of 2% nitric acid (Optima, Fisher Scientific or distilled) before analysis with inductively-coupled plasma mass spectrometry on an iCap-RQ ICP-MS (Thermo Scientific). Concentrations were then normalized using an internal standard and quantified using a multi-element standard curve. Samples where the estimated dissolved iron was < 20 nM (non-plume samples) were first pre-concentrated before analysis using a seaFAST pico column pre-concentration system (Elemental Scientific Incorporated). 10 mL of each filtered sample was pre-concentrated on a column (Nobias-1 resin) and then eluted with 500 μL of 5% nitric acid for a pre-concentration factor of 20. Eluent was then analyzed on an Element 2 ICP-MS (Thermo Scientific) and was quantified using isotope dilution for iron, copper, cadmium, zinc, nickel and lead and with standard addition for manganese and cobalt.

2.6 Hydrothermal plume detection

The ORP sensor was monitored continuously during casts for sudden changes especially coinciding with peaks in the transmissometer and bubble-like visual noise on the live multibeam feeds; these signals combined were interpreted as strongly indicative of a hydrothermal plume. The *R/V Thompson* used a hull-mounted Kongsberg EM124 deep-water multibeam echosounder operating at 12kHz.

The methods employed by this study for detecting hydrothermal plumes are specific but not sensitive; they do not exclude the potential influence of undetected plumes at other seamounts. Esmeralda, NW Rota, and Ruby have all shown signs of activity in recent years (Baker et al. 2008); only Tracey seamount is extinct (Stern et al. 2013).

2.7 ADCP

The *R/V Thompson* was hull-mounted with three Acoustic Doppler Current Profiles (ADCPs, Teledyne RD Instruments) at 75kHz (Ocean Surveyor; 5 minutes averages, 16m depth bins, depth range 28.96-972.96m), at 150 kHz (Ocean Surveyor 5 minute averages, 8m depth bins, depth range 24.93-496.94m), and at 300 kHz (Workhorse II Mariner, 2 minute averages, 2m depth bines, depth range 9.1-147.1m). ADCP instruments were configured with UHDAS (University of Hawaii Data Acquisition System).

2.8 SeaFlow

The *in-situ* shipboard automated flow-cytometer *SeaFlow* was in operation throughout the cruise (Ribalet et al., 2019). *SeaFlow* uses a stream-in-air measurement system to analyze a continuous flow of 100 μm prefiltered sweater from the *R/V* Thompson's seawater system. It measures forward light scatter (457/5- band-pass filter), phycoerythrin fluorescence (572-28 band-pass filter), and chlorophyll fluorescence (692/40 band-pass filter), binning datapoints at 3-

minute intervals. Cell size and carbon quote are estimated from light scatter assuming Mie theory for spherical particles. Cells are gated and identified as Prochlorococcus (<1 μm) Synechococcus (~1 μm), *Crocosphaera* (~ 5 μm), and other picoeukaryotes (~ < 6μm) according to Ribalet et al., 2019 (Ribalet et al., 2019).

2.9 Net Tows

At select stations overlapping with CTD cast sites a phytoplankton net (0.25m diameter, 10 or 20-μm mesh size) was deployed to the DCM for a duration of 10 minutes before recovery was initiated at 30m/min. Upon recovery the net was rinsed with saltwater before touching the deck, and the concentrated sample was refrigerated in a glass jar. During foul weather the acute angle at which the winch intersected the sea surface relative to the normal was visually estimated to calculate the true depth. Phytoplankton taxa were visually identified with the Discover Rebel compound microscope using 4x, 10x and 20x objectives with phase contrast. Sample jars were first swirled to evenly distribute settled matter before taking 1ml at a time of sample onto a gridded slide for counting. Repeated 1ml samples were counted until minimum of 300 cells were be identified. A secondary observer counted three replicates for samples using a volumetric restriction, counting only to the first 1ml.

Observer agreement on phytoplankton abundance data was tested for the three net tow samples that received multiple observers with a Bray-Curtis matrix, with the observer as the grouping variable. A Bray-Curtis matrix was also set up with the phytoplankton abundance data collected by Observer A (the primary observer) to compare differences in communities between seamounts and between seamount summit and upstream locations, and ANOSIM (n=999) was performed with this matrix using the Python Scikit-bio package.

3 Results

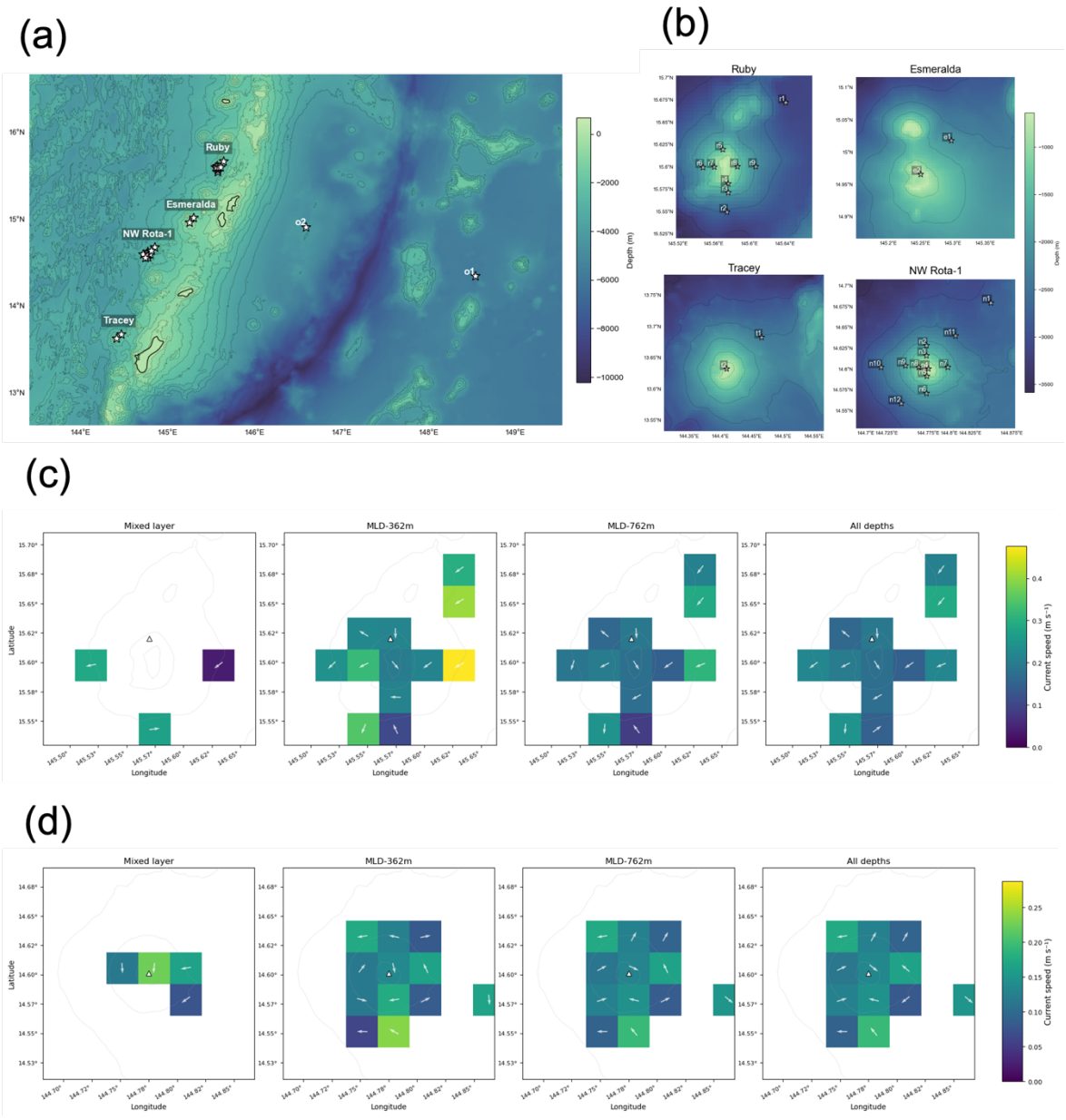

Figure 1. (a) *Map of study region with seamounts and offshore stations labeled. Stars represent transect stations. Islands are outlined in black. Background coloring depicts 15-arc second interval seafloor bathymetry from GEBCO 2025.* ***(b)*** *Clipped maps of individual seamounts. Note changes in bathymetric and cartographic scales.* ***(c-d)*** *Mean ADCP current speed (color) and direction (arrows) across varying depths at* ***(c)*** *Ruby seamount and* ***(d)*** *NW Rota-1 seamount.*

Currents were fastest at Ruby, where from the MLD-362m, mean current speed was 0.24 m/s, peaking at 0.5 m/s east of the summit between the mixed layer and 362m depth, than at Rota, where they were no faster than 0.25 m/s within any averaged depth layer (Figure 1a-b). At Ruby, current vectors beneath the mixed layer radiated largely outwards from the summit or were otherwise dominate towards the southwest (Figure 1a). At NW Rota, mixed layer current was also towards the southwest, but beneath the MLD, no dominant current flow was evident (Figure 1b).

Table 1a. Water Column Analysis (MLD, DCM, Fluor)

Activity	Seamount	Station	n	Lat	Lon	MLD	DCM	dcm_top	dcm_bottom	dcm_offset	peak_fluor	sd_fluor	int_fluor
Active	NW Rota	n2	75	14.6291	144.7727	110.3	137.2	105.3	187.2	26.8	0.160	0.087	13.186
Active	NW Rota	n3	69	14.617	144.7726	124.2	153.0	119.2	203.0	28.8	0.096	0.107	8.124
Active	NW Rota	n4	68	14.601	144.775	114.3	144.1	109.3	194.1	29.8	0.169	0.074	14.392
Active	NW Rota	n5	75	14.5922	144.7728	100.4	136.2	95.4	186.2	35.8	0.180	0.075	16.343
Active	NW Rota	n6	78	14.5717	144.7727	107.3	142.1	102.3	192.1	34.8	0.166	0.083	14.910
Active	NW Rota	n8	70	14.6027	144.763	112.3	139.1	107.3	189.1	26.8	0.126	0.094	10.348
Active	NW Rota	n9	66	14.6047	144.7475	111.3	139.1	106.3	189.1	27.8	0.172	0.068	14.324
Active	NW Rota	n10	59	14.6028	144.718	127.2	136.2	122.2	186.2	8.9	0.149	0.069	9.546
Active	NW Rota	n12	76	14.5594	144.74213	122.2	152.1	117.2	202.1	29.8	0.126	0.079	10.746
Inactive	Esmeralda	e2	64	14.9667	145.25	114.3	129.2	109.3	179.2	14.9	0.211	0.134	14.823
Inactive	Tracy	t2	89	13.633	144.41	97.4	133.2	92.4	183.2	35.8	0.196	0.101	17.838
Inactive	Ruby	r2	87	15.55	145.575	116.3	159.0	111.3	209.0	42.7	0.397	0.124	38.859
Inactive	Ruby	r3	95	15.5721	145.5761	108.3	150.1	103.3	200.1	41.7	0.450	0.100	43.576
Inactive	Ruby	r4	84	15.582	145.5761	115.3	150.1	110.3	200.1	34.8	0.439	0.120	39.429
Inactive	Ruby	r5	86	15.62	145.57	99.4	134.2	94.4	184.2	34.8	0.426	0.085	38.229
Inactive	Ruby	r6	82	15.6004	145.548	118.3	148.1	113.3	198.1	29.8	0.404	0.097	34.193
Inactive	Ruby	r7	97	15.6005	145.5607	99.4	149.1	94.4	199.1	49.7	0.409	0.087	42.777
Inactive	Ruby	r8	96	15.6009	145.5867	114.3	164.0	109.3	214.0	49.7	0.392	0.099	40.990
Background	Esmeralda	e1	58	15.0186	145.2976	105.4	119.3	100.4	169.3	13.9	0.159	0.102	10.986
Background	Ruby	r1	67	15.6726	145.6404	117.3	139.1	112.3	189.1	21.9	0.371	0.123	28.525
Background	NW Rota	n1	71	14.6804	144.8498	105.4	126.2	100.4	176.2	20.9	0.167	0.069	12.765
Background	Offshore	o1	79	14.3495	148.5396	131.2	161.0	126.2	211.0	29.8	0.160	0.108	13.626
Background	Offshore	o2	73	14.9151	146.5928	114.3	134.2	109.3	184.2	19.9	0.171	0.123	12.844

Table 1b. Water Column Summary by Seamount

Group	n	MLD	DCM	Peak Fluor *(mg/m^3)*	Int. Fluor *(mg/m^2)*
Esmeralda	2.00	111.8 ± 3.5	124.2 ± 7	0.185 ± 0.037	12.9 ± 2.71
NW Rota	11.00	112.9 ± 8.4	139.2 ± 8.7	0.152 ± 0.026	12.42 ± 2.53
Offshore	2.00	117.8 ± 4.9	147.6 ± 19	0.165 ± 0.008	13.24 ± 0.55
Ruby	8.00	114.2 ± 8.5	149.2 ± 9.6	0.411 ± 0.026	38.32 ± 4.92
Tracy	1.00	97.4	133.2	0.196	17.84
ALL	24.00	111.8 ± 21.5	141.7 ± 11.6	0.244 ± 0.123	21.39 ± 12.7
min		*97.41*	*124.20*	*0.165*	*12.90*
max		*117.8*	*149.2*	*0.411*	*38.32*
range		*20.4*	*25.0*	*0.246*	*25.42*

Table 1c. Water Column Summary by Seamount Activity

Group	n	MLD	DCM	Peak Fluor *(mg/m^3)*	Int. Fluor *(mg/m^2)*
Active	9.00	114.4 ± 8.7	142.1 ± 6.5	0.149 ± 0.028	12.44 ± 2.82
Inactive	9.00	114.7 ± 10.6	136 ± 15.9	0.206 ± 0.093	15.75 ± 7.21
Background	5.00	109.2 ± 8.3	146.3 ± 11.9	0.369 ± 0.096	34.52 ± 10.7
ALL	23.00	112.4 ± 8.9	142.4 ± 11.3	0.248 ± 0.125	21.8 ± 12.82
min		*109.20*	*136.00*	*0.15*	*12.44*
max		*114.40*	*146.30*	*0.37*	*34.52*
range		*5.20*	*10.30*	*0.22*	*22.08*

307

Table 1d. One-Way ANOVA Results for Water Column Environmental Variables

Grouping	MLD		DCM		Integrated Fluorescence		Peak Fluorescence		DCM Offset	
	F-statistic	P-value	F-statistic	P-value	F-statistic	P-value	F-statistic	P-value	F-statistic	P-value
Activity	0.96	0.40	1.40	0.27	20.48	1.45E-05	20.04	1.67E-05	5.74	0.01
Seamount	1.68	0.20	3.35	0.03	63.19	2.39E-10	117.74	1.20E-12	4.36	0.01

308

(a)

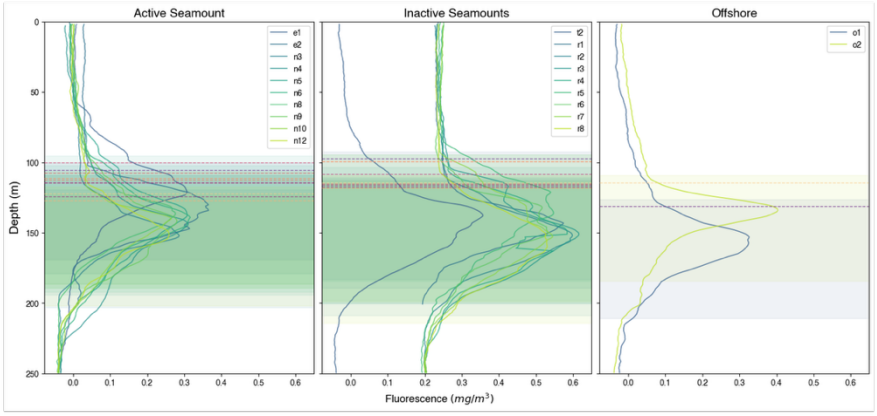
Active Seamount
Inactive Seamounts
Offshore
Depth (m)
Fluorescence (mg/m³)

(b)

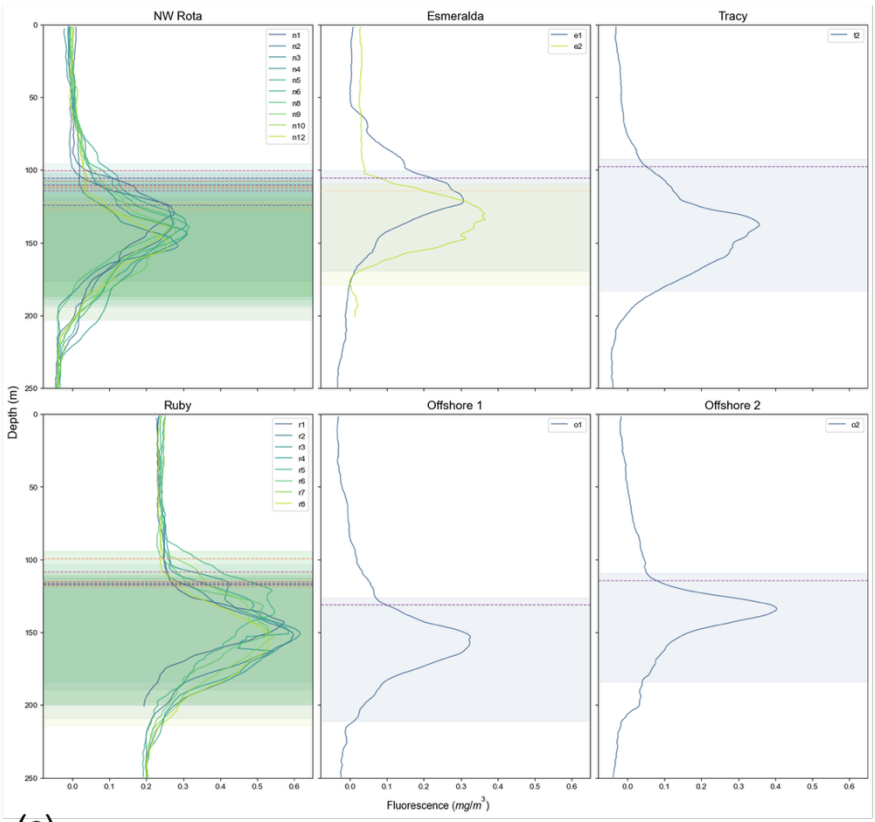
NW Rota
Esmeralda
Tracy
Ruby
Offshore 1
Offshore 2
Depth (m)
Fluorescence (mg/m³)

(c)

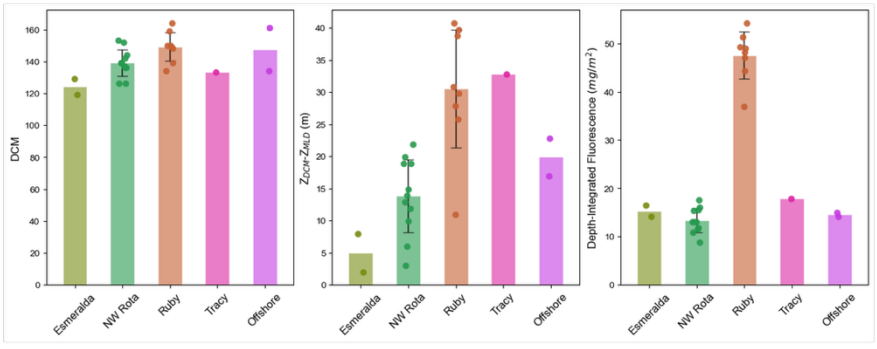
DCM
Depth-Integrated Fluorescence (mg/m²)
Esmeralda
NW Rota
Ruby
Tracy
Offshore

309

Figure 2. (**a)** Vertical fluorescence profiles by station and seamount or offshore location, inferring chlorophyll as mg/m^3. Change in station color reflects transect across summit (see station legend and Figure 1 for maps). The correspondingly colored shaded bands span the area over which depth-integrated fluorescence was estimated. Dashed warm-colored lines represent the MLD for each fluorescence profile. Profiles were smoothed with a rolling average across every ten samples to reduce visual noise. **(b)** Identical profiles in (2a), organized by seamount activity status. **(c)** Summary bar plots of the same data from Figure 2a showing DCM, Z_{DCM}-$Z_{MLD,}$ and depth-integrated fluorescence across seamounts. Individual stations are overlaid as points. Offshore stations are o1 and o2. Error bars represent the standard deviation. The depth of the DCM (Z_{DCM}) was defined as 50m beneath the peak fluorescence recorded at that location. Z_{DCM}-Z_{MLD} represents DCM offset beneath the MLD; positive values mean the DCM was beneath the MLD.

The ranges and means for the MLD, DCM, Z_{MLD} - Z_{DCM} (DCM offset), peak fluorescence, and integrated fluorescence across stations and station grouping categories are displayed in Table 1a-c. The DCM was beneath the MLD at all stations. The ranges of the MLD, DCM, and DCM offset were 97-131m (range: 34m), 119-164m (range: 45m), and 9-50m (range: 40m), respectively. The mean MLD was 112.4 m ± 8.94 and the mean DCM was 142 m ± 11.32 (Table 1a). Regardless of categorical grouping regime, the mean MLDs were within one standard deviation of each other (Table 1b-c).

Separating stations according to summit proximity instead of by seamount produced a fourfold larger spread in MLD values and the lowest F-statistic of 0.96 ($p = 0.4$) (Table 1b-d).

Variance in fluorescence was higher between seamounts or between activity grouping than between the set of stations within an individual seamount (Figure 2a-b). One-way ANOVA performed on both grouping methods produced significant F-statistics for integrated fluorescence of 20.48 ($p < .0005$, by activity status) and 63.19 ($p <.0005$, by seamount) (Table 1d). Both the peak (0.411 ± 0.026 *mg/m³*) and depth-integrated (38.32 ± 4.92 *mg/m²*) fluorescence at Ruby seamount were threefold higher than at any other seamounts or offshore locations (Table 1b). Peak and depth-integrated fluorescence were similar across stations, validating the use of

depth-integrated fluorescence as the more robust of the two as a chlorophyll proxy. A post-hoc Tukey test was performed on integrated fluorescence with p = < .0005 for Ruby seamount in all pairwise comparisons; all other pairings had p > 0.05.

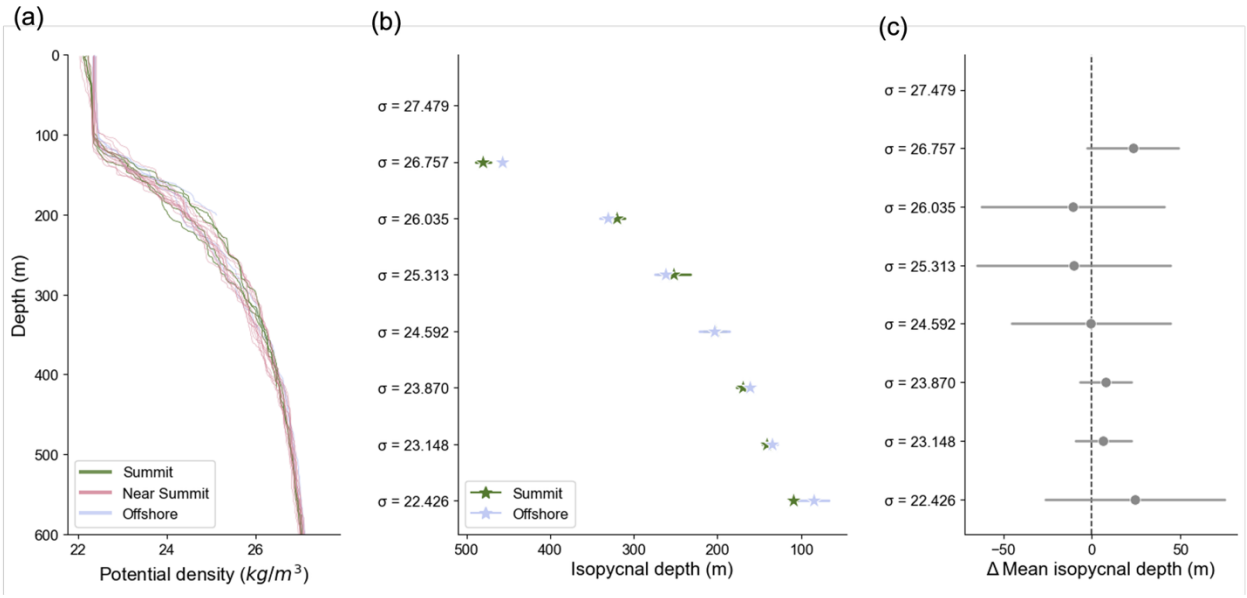

Figure 3. (**a)** Vertical density profile at upstream, summit, and near summit stations across all seamounts. **(b)** Mean depth at summit (n=4) vs. off-summit (n=5) stations of six staggered density isopycnals between 100 and 500m, with error bars showing 95% C.I. **(c)** Mean difference in isopycnal depth over summit, where negative values represent doming and positive values represent depression. Welch's t-test was used to determine significance of isopycnal offset based on summit proximity.

The mean depth differences of six isopycnals from 100-500m were calculated at summit and offshore stations, ranging from -10.32m to +24.41m. No statistically significant isopycnal doming or depression was detected at any seamount between summit and offshore stations (Welch's t-tests, n=2-4, p > 0.05 for all). All isopycnal differences were within the 95% confidence intervals (Figure 3c) All confidence intervals included a change of sign in the depth difference, indicating no consistent directionality toward either doming or depression between stations grouped by summit proximity.

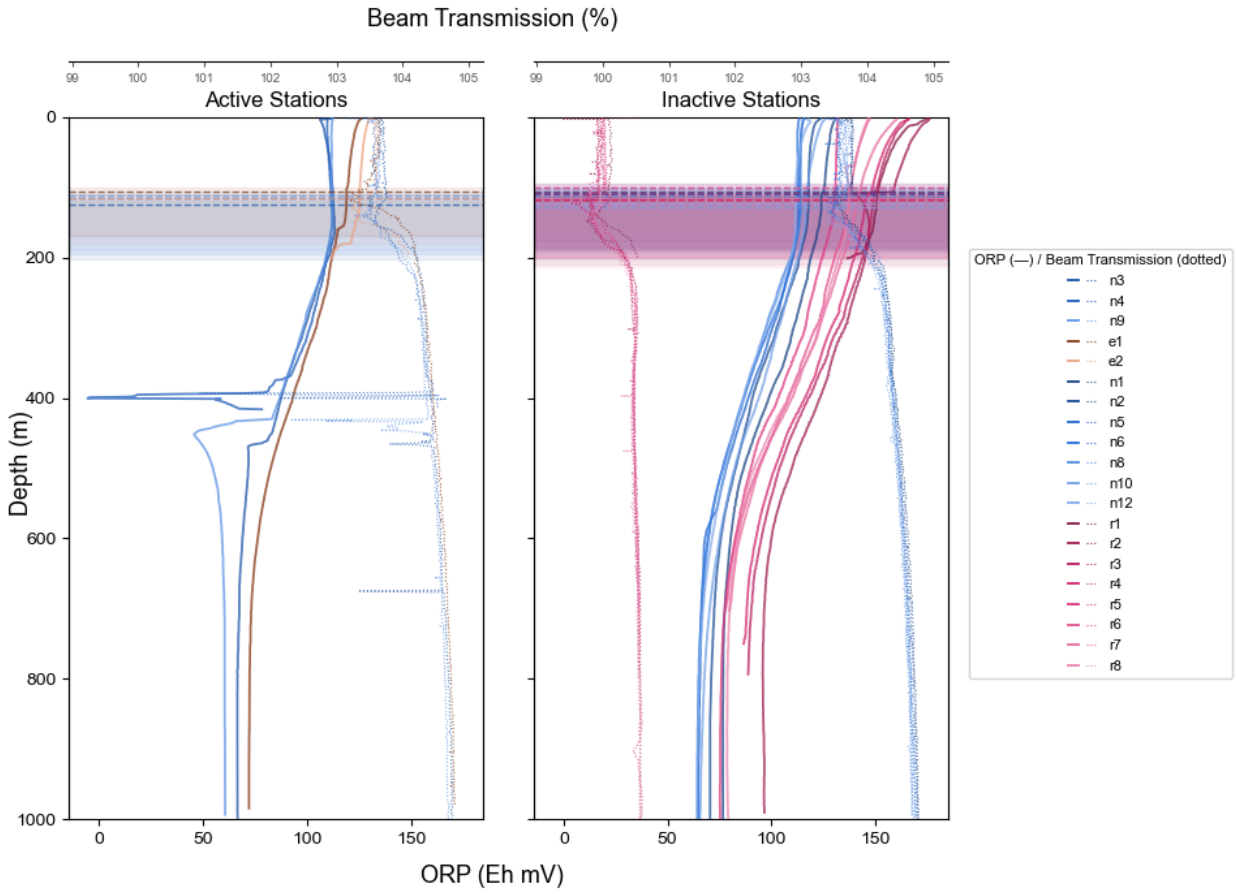

Figure 4. Eh (unitless) from ORP sensor and beam transmissometer (% transmission) profiles separated by seamount and according to plume characteristics in the signal. Stations within seamounts share hues and differ in shade. Values <0.1 on the ORP sensor were excluded.

Plumes were detected at NW Rota stations n3, n4, and n9, (but particularly n3) where rapid changes to Eh occurred between 400 and 450m, indicative of reducing fluids, accompanied by spiked decreases in beam transmission at matching depths (Figure 4). At n3, visual artifacts associated with plume bubbling appeared on the multibeam at the same time. At Esmeralda, there were subtler excursions in Eh and beam transmission at 150-200m (Figure 4). Beam

transmission was 3% lower at Ruby seamount than at other stations (Figure 4).

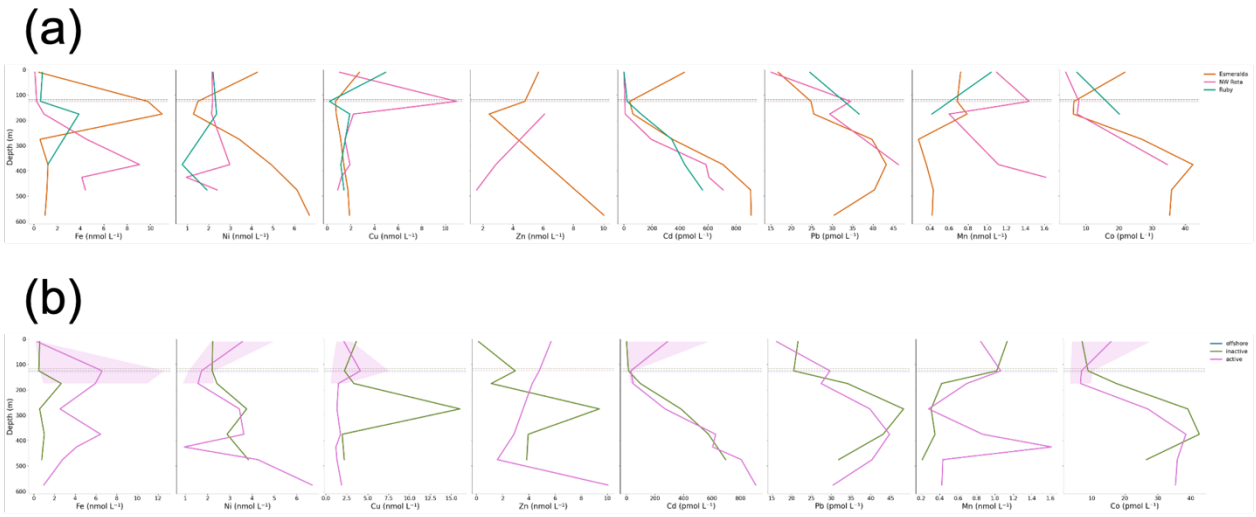

Figure 5. (a) Depth-binned depth-averaged nutrient profiles at Esmeralda, NW Rota, and Ruby **(c)** Depth-binned depth-averaged nutrient profiles by seamount activity status.

At NW Rota, dFe and dMn were elevated at concurrent depths and stations where particulate hydrothermal plumes were indicated by Eh and turbidity excursions. At n2, dFe was elevated to 17nM (400m) and 5nM (450m); background dFe was <2nM. At n3, dMn was fourfold higher at ~2nM (at 400m) relative to background, which displayed the typical scavenged depth profiles of Mn < 0.5nM beneath the DCM (Figure 5). At Esmeralda summit station e2, dFe was highly elevated (15-35nM) in samples taken just beneath the DCM at (Figure 5).

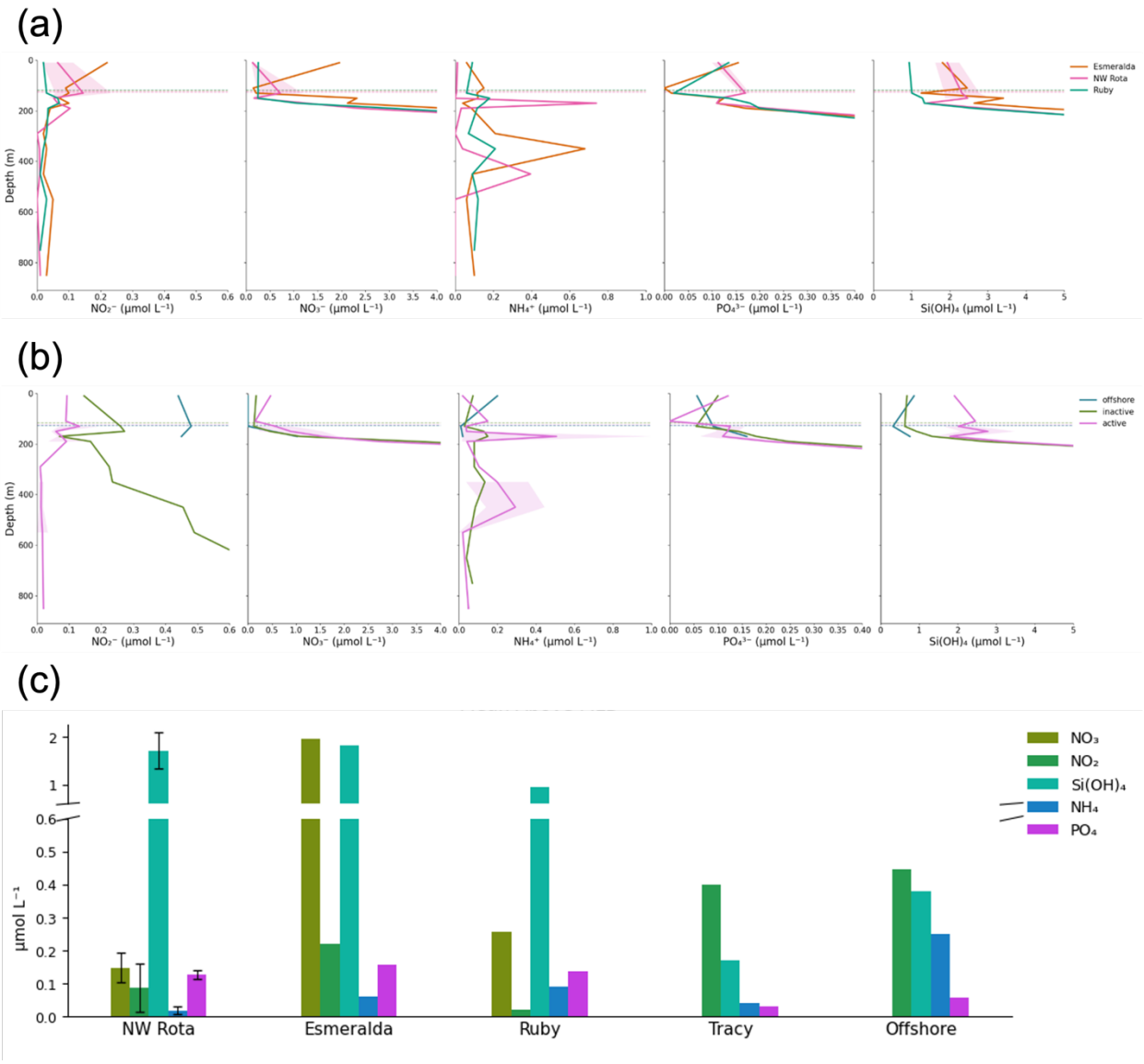

Figure 6. (**a**) Depth-binned nutrient profiles between offshore, active (NW Rota and Esmeralda), and inactive (Ruby and Tracey) seamounts. **(6b)** Depth-binned nutrient profiles between individual seamounts: NW Rota, Esmeralda, and Ruby. **(6c)** Mean mixed layer nutrient concentrations by seamount (depth<MLD).

Mixed layer nutrient concentrations varied considerably across seamount, but only differences in $Si(OH)_4$ and NH_4 were statistically significant ($Si(OH)_4$: F=4.7, p=0.03; NH_4: F=4.9, p=0.03, one-way ANOVA). Offshore and Tracey stations had both the highest NO_2 (0.44 µM offshore and 0.40 µM at Tracey) and undetectable NO_3 (Figure 6). At stations with

386 measurable NO_3 (i.e., Ruby, NW Rota, and Esmeralda), it was either first or second most
387 concentrated (maximum 1.96 μM at Esmeralda) alongside $Si(OH)_4$ (maximum 1.82 μM at
388 Esmeralda) while all other nutrients at these seamounts were < 0.25 μM (Figure 6c). Esmeralda
389 had the most nutrient-enriched surface layer overall and the highest individual concentrations of
390 NO_3, $Si(OH)_4$, PO_4 (Figure 6c).

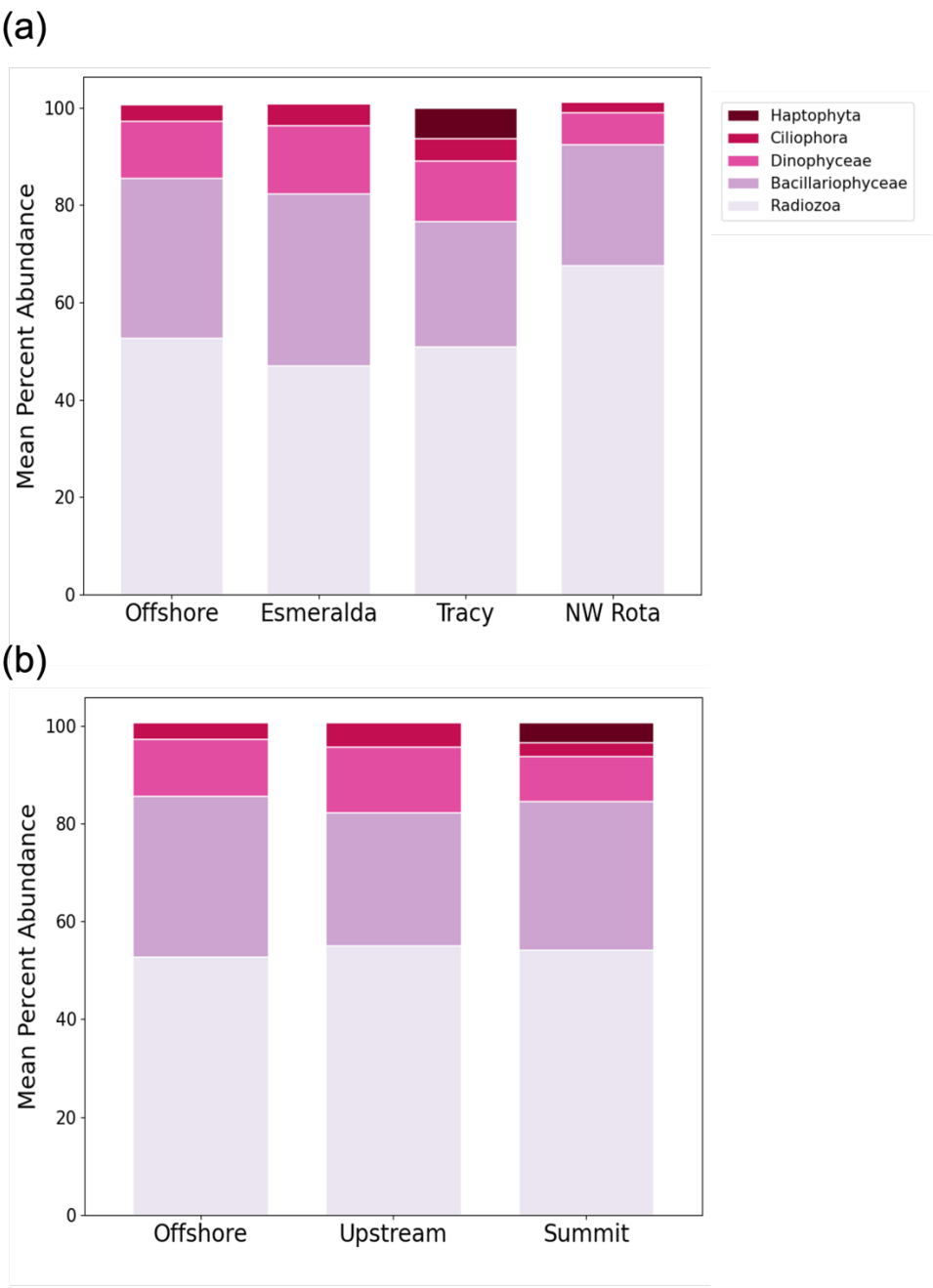

391

392 **Figure 7.** Weighted average percent abundance of major phytoplankton taxa and zooplankton *Radiozoa* by **(a)**
393 Seamount or offshore location, and **(b)** upstream of seamount, seamount summit, or offshore station. n = 2,444 cells
394 counted over n = 8 stations. Approximately 300 cells were counted at each station.

395

396 The four major plankton taxa consistently identified in net tow samples at the DCM were
397 Radiozoa, Bacillariophyceae, Dinophyceae, and Ciliophora. Haptophyta was also sporadically
398 identified, but differential identification between Haptophyta and Radiozoa was tenuous as both
399 were mostly found in aggregated particles that obscured visual identification. Rare taxa ($n < 10$)
400 identified at each station were excluded from the analysis due to a lack of visual replicability
401 producing high uncertainty in their identification.
402 2,444 cells were identified in total by observer A, and three stations (e1, e2, n4)
403 comprising 418 cells received replicate counts by observer B. Disagreement in station counts
404 between observers was larger than between stations or seamounts, regardless of grouping
405 variable (upstream/downstream, plume/no plume, seamount/offshore) (Table A1, Table A3).
406 When observers were used as grouping variables for stations e1, e2, and n4, the mean Bray-
407 Curtis dissimilarity was 0.51, exceeding the mean Bray-Curtis dissimilarity of 0.158 in the
408 primary analysis using seamounts as grouping variables (Table A2, Table A4). Despite this
409 disagreement, both observers identified Radiozoa, Bacillariophyceae, Dinophyceae, and
410 Ciliophora as the most abundant across every station. (Table A3).
411 For all samples examined by observer A, the ranks of taxon abundance were invariant by
412 station, in order of descending relative abundance: Radiozoa, Bacillariophyceae, Dinophyceae,
413 Ciliophora, Haptophyta (Fig 4). ANOSIM was performed on a Bray-Curtis dissimilarity matrix
414 using stations within each seamount as replicates and seamounts as groups, producing an R-
415 statistic of 0.333 indicating similarity, but the p-value was not significant ($p = 0.143$), likely due
416 to the small number of stations per seamount (Table 2b).

417

(a)

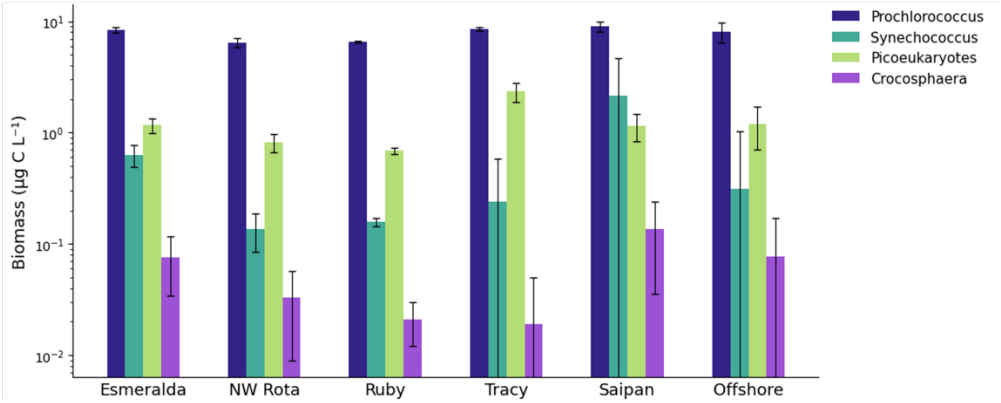
Prochlorococcus
Synechococcus
Picoeukaryotes
Crocosphaera
Biomass (µg C L⁻¹)
Esmeralda
NW Rota
Ruby
Tracy
Saipan
Offshore

(b)

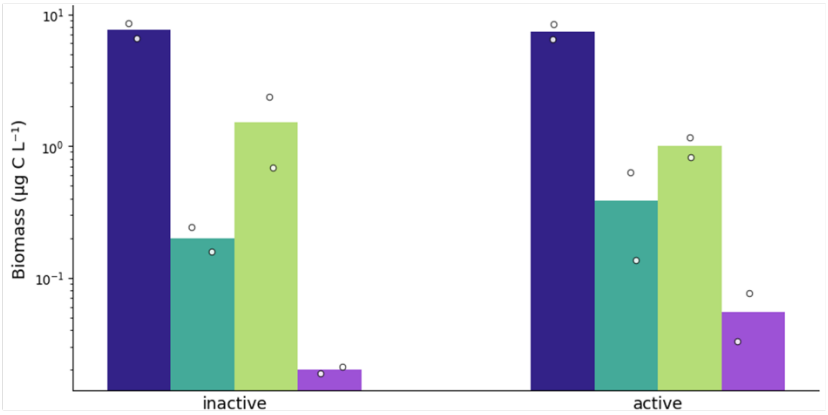
Biomass (µg C L⁻¹)
inactive
active

(c)

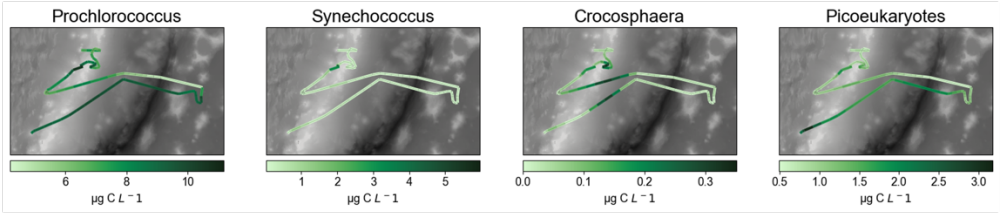
Prochlorococcus
Synechococcus
Crocosphaera
Picoeukaryotes
µg C L⁻¹

(d)

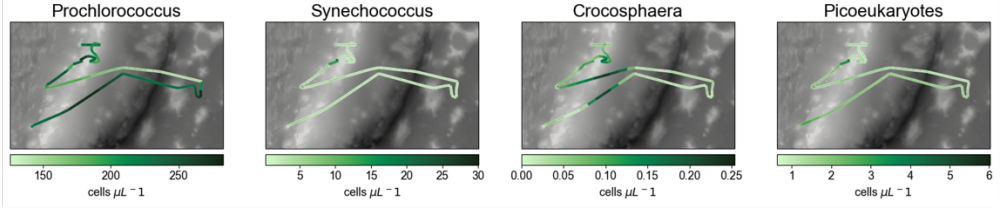
Prochlorococcus
Synechococcus
Crocosphaera
Picoeukaryotes
cells µL⁻¹

418

Figure 8. (8a) Inter-seamount comparison of mean biomass (µg C L^{-1}) of surface pico- and nano-phytoplankton detected by *SeaFlow*. Means are aggregated from hourly means of continuous data recorded during the transect: all hourly means within 15km of each summit are assigned to that summit and classified offshore if not (also excluding points 15km away from the island of Saipan). Error bars represent the mean SD from hourly means. **(8b)** Mean *SeaFlow* biomass categorized by site type. Jittered dots represent the values displayed in **(8a)**; the value of the bar is their mean. **(8c-d)** Biomass (µg C L^{-1}) **(8c)** and abundance (cells μL^{-1}) of *Prochlorococcus, Synechococcus, Crocosphaera,* and other picoeukaryotes measured by *SeaFlow* during ship transect.

Total surface nano- and picoplankton biomass did not differ significantly across study sites. One-way ANOVA was compared changes in biomass between active seamounts NW Rota (n = 8) and Esmeralda (n=2), inactive seamounts Ruby and Tracey (n = 6), and offshore stations (n=3). Only *Crocosphaera* biomass differed significantly across site types ($F = 5.51$, $p = 0.035$) (Figure 8c). A post-hoc Tukey test revealed a significant decrease in *Crocosphaera* at active seamounts relative to inactive seamounts, while statistical power was impaired in pairwise tests with offshore stations by low n ($n = 3$) offshore (Figure 8c). However, this difference grew stronger with increased distance thresholds from seamount summits, reflecting the increases in *Crocosphaera* east of these seamounts, potentially a zonal gradient not related to the seamounts themselves, but to larger-scale circulation and nutrient patterns at this location (Figure 8c-d).

4 Discussion

4.1 300% chlorophyll enhancement at Ruby suggests high variability over small timescales

Spatially significant chlorophyll did not occur within seamounts relative to summits, but between seamounts. Depth-integrated chlorophyll was elevated threefold at all Ruby seamount stations (mean: 38.2 mg/m^2), a clear increase not observed in any other stations or seamounts: At

NW Rota, Esmeralda, and offshore, mean integrated chlorophyll ranged from 12.9 to 13.24 mg/m^2; while it was slightly significantly elevated at Tracey (17.84 mg/m^2) (Table 1b). This difference at Ruby was statistically validated in every pairwise Tukey test ($p < 0.0005$) and was within the predicted two-to-fourfold magnitude of chlorophyll enhancement.

At the nearby C4 seamount, Dai et al. recorded an average depth-integrated chl *a* of 11.84 mg/m^2, comparable to our measurements at NW Rota, Esmeralda, and offshore (Dai et al. 2020). Yet within this average at the C4 seamount, chl *a* at the DCM was elevated from 0.1mg/m^2 to 0.15 mg/m^2 at the summit or along the flanks most proximal to the summit (depending on the transect) relative to flank locations distal from the summit, a 1.5-fold increase indicating a localized seamount-summit effect, observed concurrently with isopycnal doming (Dai et al. 2020). Taken together, these findings point to distinct circulation mechanisms behind summit-localized and seamount-generalized chlorophyll enhancements.

Furthermore, the 300% depth-integrated chlorophyll increase at Ruby seamount measured during a single day contextualizes previous work (Leitner et al. 2020) using satellite datasets to model the decadal and monthly averages of seamount-induced chlorophyll enhancements (or SICE's) across the entire Pacific. Fitting surface chlorophyll with seafloor depth, the decadal average SICE was 5% with a maximum of 35%, and these values increased as the temporal scale decreased, up to a maximum of 56% during the month of February across all years (Leitner et al. 2020). The much greater increase observed here at Ruby seamount within a single day better contextualizes the variability in primary productivity at small temporal scales contributing to milder averages in larger datasets (Leitner et al. 2020). This finding motivates future work to determine the mechanisms driving the magnitude and variability of chlorophyll in seamount-dense oligotrophic ocean regions across. They indicate the need to further understand

466 the implications of such patchiness in primary productivity, which can cascade up the food web
467 to fish, where greater catch diversity was also associated with SICE's (Leitner et al. 2020). It
468 remains unclear how sensitive measures of biomass across trophic levels may be to such
469 dramatic patchiness in primary productivity.

470 Broadly, seamount-induced circulation changes include mesoscale eddies or internal
471 tides, forming anticyclonic gyres or stimulating vertical overturn and particle advection and
472 retention around seamounts (White 200). Increased chlorophyll at the DCM can occur as a result
473 due to retention of existing phytoplankton around a seamount nourished on allochthonous
474 nutrients, or due to nutrient circulation from enhanced turbulent mixing over seamount flanks
475 (Toole et al. 1997). The latter can be detected through isopycnal doming and transect coverages
476 at Ruby and NW Rota were of comparable resolution to previous work which positively
477 identified doming (Dai et. al 2020, 2022). Yet isopycnal analysis between summit and off-
478 summit stations revealed no evidence of doming at any seamount (Welch's t-test, $p > 0.05$) and
479 consistent density structures overall, surprising given the variation in both chlorophyll and
480 DCM-offset from MLD (Figure 3, Table 1). The lack of evidence for doming points to
481 alternative mechanisms of topographic forcing or biological patchiness as explanations for the
482 chlorophyll anomaly at Ruby. Such mechanisms are also implicated in the current dynamics
483 around Ruby, in the form of the observed faster currents and their outward-radiating directions
484 beneath the mixed layer, which suggest upwelling not detected by isopycnal restructuring as a
485 more likely mechanism than particle retention.

486 Sensor calibration issues between fluorescence and chlorophyll are another potential
487 explanation and should be noted, as there were problems with shipboard laboratory chlorophyll
488 extraction leading to reliance for this study on fluorescence as a chlorophyll proxy.

4.2 Bioavailability of hydrothermal plumes in the euphotic zone

Evidence for a buoyant hydrothermal plume at NW Rota was strongest between 400-450m at n3, while additional plume signals were detected around these depths at n4 and n9, justifying the classification of NW Rota summit stations as active stations. A 2007 survey of NW Rota also detected the most intense plumes at 460m of depth in the same locations (Resing et al. 2007). At this depth, the plume is separated from the euphotic zone by the last 300m of the pycnocline, placing it in a distinct, if adjacent, water mass. Many processes govern the diapycnal mixing of plume waters and the distribution, dissolution, uptake, adsorption, or precipitation of trace metal species enriched in those waters. Fe(II) readily precipitates to Fe(III) or is complexed into Fe-sulphides and Fe-oxyhydroxides, but significant quantities are also stabilized by organic ligands to remain in the dissolved form, where they may be transported thousands of kilometers, undergoing dispersion though not precipitation (Resing et al. 2015). While it is plausible that plumes at this depth are a source of bioavailable Fe to the euphotic zone, in the absence of vigorous mixing, such effects are likely to manifest elsewhere or across a larger spatial scale representing a more dilute Fe source.

The extremely elevated dFe at Esmeralda (15-35nM) are suggestive of shallow (150-200m) and more diluted plume-enriched waters with a decreased concentration of particles or reducing fluids reflected by the decreased transmission and Eh signal. At Esmeralda, dFe was sampled at 170-200m so it is likely available to the euphotic zone. The compensation depth Z_c marking the base of the euphotic zone could not be calculated from PAR (i.e., $Z_{\sim 0.5\%}^{PAR}$) due to a malfunctioning PAR sensor, but it is reasonable to assume it lies just beneath the DCM, as this pattern has been previously demonstrated (Leach et al. 2018, Fennel & Boss 2003, Tett et al. 2002, Scofield et al. 2020).

4.3 Potential impacts of shallow plume-derived iron and silica on phytoplankton communities and productivity in an oligotrophic region: directions for future research

At active seamounts, $Si(OH)_4$ was significantly elevated throughout the mixed layer alongside significant increases in NH_4 between the base of the MLD and the DCM. Both NW Rota and Esmeralda showed anomalously elevated surface $Si(OH)_4$ (~1.75 and ~1.82 µmol L^{-1}, respectively) relative to Tracy and offshore stations (~0.20 and 0.40 µmol L^{-1}, respectively), and intermediately elevated silicate at Ruby (~ 1.0 µmol L^{-1}). Resing et al. (2009) surveyed hydrothermal plumes across 50 Mariana Arc volcanoes and found strong chemical anomalies over active summits, including silica as a signature of hydrothermal fluids. This surface $Si(OH)_4$ anomaly at NW Rota is first parsimoniously interpreted as a diluted expression of hydrothermally enriched subsurface water. $Si(OH)_4$ is used a conservative plume tracer (Pichler et al. 1999, Lin et al. 2020)—and here, it is indeed elevated at all depths compared to inactive seamounts.

However, direct input of $Si(OH)_4$ from a plume is insufficient to characterize the observed shifts in mixed layer nutrients. Within the euphotic zone, $Si(OH)_4$ is readily assimilated by siliceous phytoplankton, especially diatoms, but despite its bioavailability it was still conserved throughout the mixed layer. It is well-documented that the typical $Si(OH)_4$:NO_3 ratio increases when cells are stressed for iron, relative to nutrient-replete conditions (Brzezinski 1985). At inactive seamounts, our measured dFe values were within the range shown to increase the $Si(OH)_4$:NO_3 uptake ratio (Shaked et al. 2021, Brzezinski et al. 2003). And in the context of the extremely elevated dFe near the DCM at Esmeralda, the elevated $Si(OH)_4$points to Fe-fertilization that releases silicic acid from a state of secondary nutrient limitation that may be occurring at the Fe-depleted inactive seamounts. Iron limitation and secondary silicic acid

limitation (i.e., taxa specific limitation) occurs beyond only the well-studied HNLC ocean in coastal upwelling regions (Hutchins and Bruland 1998). Seawater incubation experiments in these regions also suggest that NO_3 assimilation is more tightly regulated by Fe availability than $Si(OH)_4$ (Takeda 1998, Hutchins and Bruland 1998). Comparing the values of NO_3, NH_4 at active and inactive stations with the predicted changes in growth rates across nutrient gradients of N and Fe assuming Michaelis–Menten uptake dynamics calculated in Browning et al. 2017, shifts in this study region from N-limiting oligotrophic conditions towards serial or co-limitation of N and Fe may be occurring between at those stations near plumes where elevated N was observed (Browning et al. 2017).

4.4 No detectable differences in relative abundance of major plankton taxa at the DCM regardless of chlorophyll enhancement or hydrothermal plume influence

Despite multiple stations exhibiting elevated trace metals probably derived from hydrothermal plumes and threefold elevated chlorophyll at Ruby seamount, the plankton community according to observer A at the DCM for every station was characterized by the same rank order of taxon abundance; in descending order: Radiozoa, Bacillariophyceae, Dinophyceae, Ciliophora, Haptophyta. However, inter-observer dissimilarity (Bray-Curtis = 0.51) exceeded inter-station dissimilarity (Bray-Curtis = 0.158). Inter-observer analysis only validated the detection of all taxa at all sites, but not the invariant rankings of taxa found by the primary observer. Variability in results between observers was primarily due to differences in the identification of the two most abundant taxa, Radiozoa and Bacillariophyceae.

Cells were identified between 4-20x magnification, so these data sampled only cells > ~ 10μm with a skew towards much larger cells as small ones were easier to miss and were more easily hidden hide inside particulate debris on the slide. Radiozoa and Haptophyta were

associated primarily in aggregated particles, obscuring identification, they also introduced sampling patchiness as these clumps could not be effectively broken up via swirling without risk of damaging the cell structures past the point of identification. These data indicate that any effect size was not detectable within the resolution scale of the study design (e.g., number of stations, number of cells, taxonomic level of identification). These data do not rule out potential facultative behavior in response to pulsed metal inputs in rarer species or at smaller size classes but indicate the need for more robust identification methods and larger sample sizes to detect any such responses.

5 Conclusions

This study partially supports the hypothesis that topographic forcing at seamounts produces measurable increases in phytoplankton biomass at the surface but did not find evidence for the prediction that hydrothermal plumes drive shifts in major taxon relative abundance at the DCM. The threefold elevation in depth-integrated chlorophyll at Ruby seamount is consistent with the high inter-seamount variability and small-scale patchiness suggested by broader Pacific Ocean satellite-based datasets examining seamount-associated chlorophyll enhancements (Leitner et al. 2020). Isopycnal doming was not present as a mechanistic explanation, though faster, outward-radiating ADCP currents at Ruby suggest topographic influence occurring. This finding warrants further research into the physical mechanisms that may drive upwelling at seamounts, as well as temporal variability of this spatial patchiness.

At NW Rota and Esmeralda, surface NO_3 and $Si(OH)_4$ — the latter consistent with hydrothermal fluid signatures documented in Mariana Arc volcanoes and used as a conservative tracer of hydrothermal plumes more broadly (Resing et al. 2009, Lin et al. 2020, Pichler et al. 1999)—were associated with increases in the diazotrophic cyanobacteria *Crocosphaera*

alongside increased NH_4. Further work is needed to understand the drivers of the observed zonal gradients in *Crocosphaera* along zonal transects between the Mariana arc and trench and further clarify their ecological relationship between diazotrophic and siliceous phytoplankton in these periodically plume-enriched oligotrophic waters.

Despite seamount-associated shifts in fluorescence (at Ruby) and metals and nutrients at active seamounts (NW Rota, Esmeralda), there were no detectable shifts in the structure of phytoplankton communities at the DCM. Although limited by inter-observer inconsistencies, these data support the consistent presence of all four most abundant taxa (Radiozoa, Bacillariophyceae, Dinophyceae, and Ciliophora) at all stations, establishing a baseline for future work and the need for higher spatial and taxonomic resolutions to resolve potential community responses.

Acknowledgments

I would like to extend an enormous thank you to the wonderful captain and crew of the *R/V* Thompson*;* to my classmates for their support in data collection, cleaning, and peer-reviews; to Rachel Ha for her help with code and as a secondary observer identifying plankton in my net-tow samples; to the plankton, too, for being so beautiful; and finally, to the professors of the University of Washington senior thesis course sequence OCEAN 443/444/445: Randie Bundy, Andrea Ogston, Ginger Armbrust, Alison Gray, and my thesis mentor, François Ribalet, for all of their incredible support and encouragement. This research was funded by the Department of Oceanography at the University of Washington.

Appendices

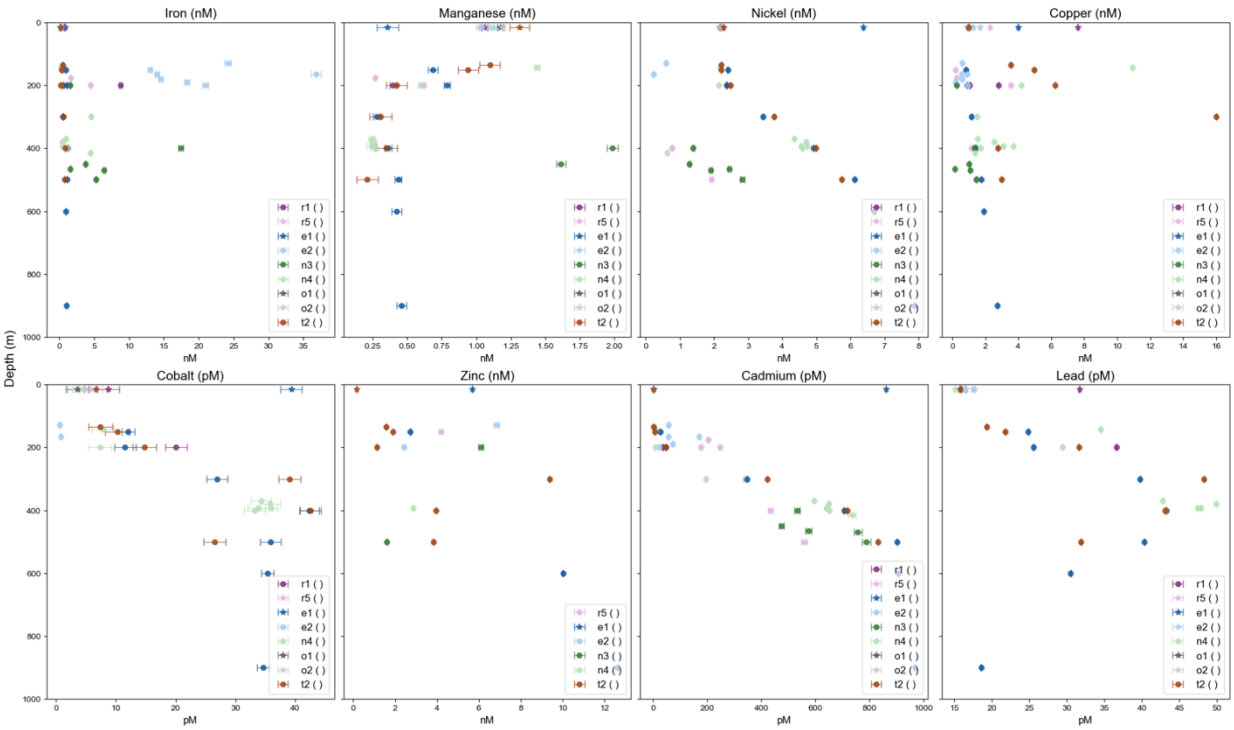

Figure A1. Vertical depth profiles of all dissolved metals. Each subplot shows all datapoints collected for that metal. Stars indicate samples from the trace metal clean pump at 15m depth. Circles indicate samples from CTD Niskin bottles. Symbols of the same hue with different saturation indicate stations at the same seamount, while different hues indicate different seamounts.

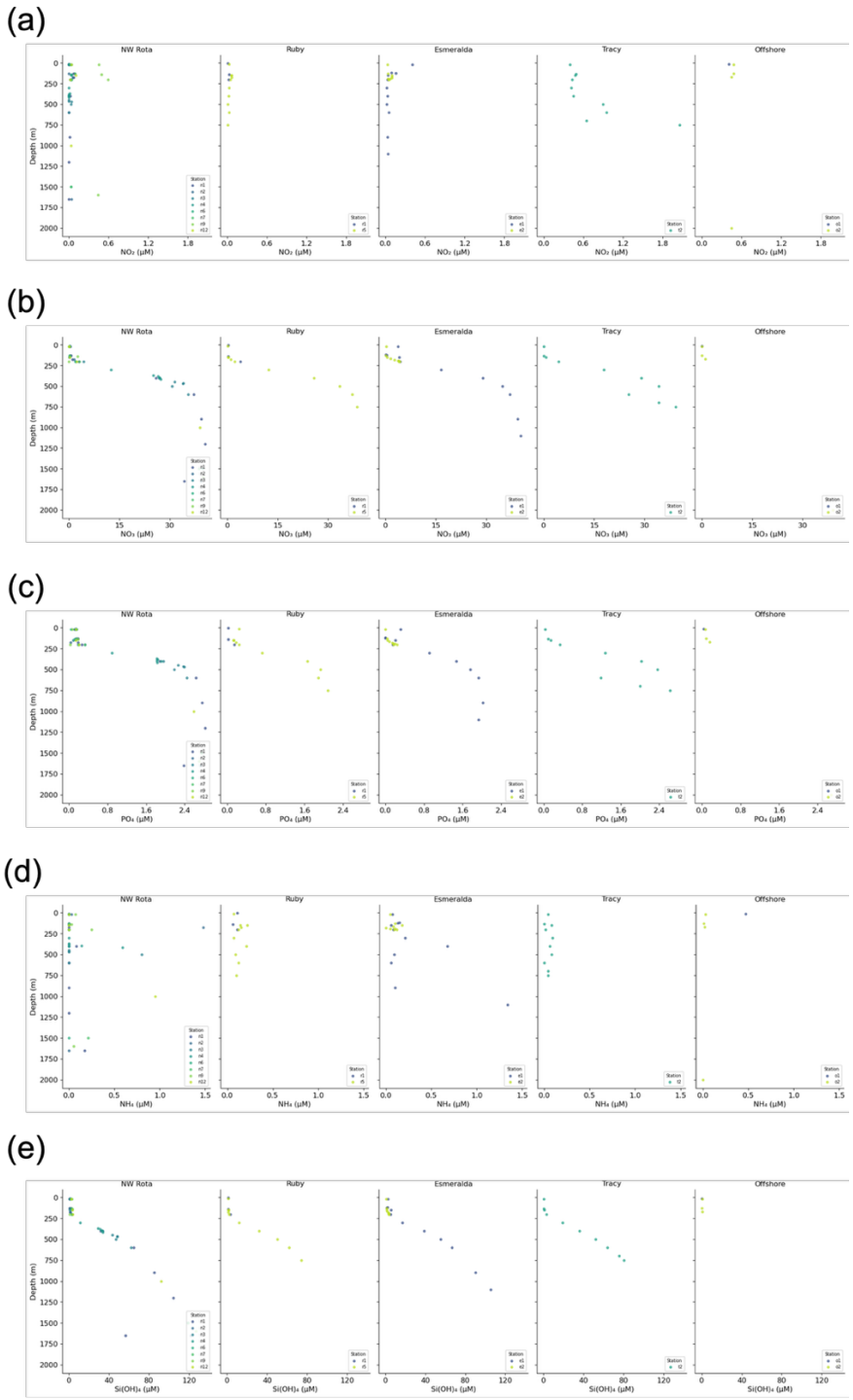

Figure A2. Vertical nutrient profiles organized by seamount. Each row contains data for a given nutrient analyte: **(a)** nitrite, **(b)** nitrate, **(c)** phosphate, **(d)** ammonium, **(c)** orthosilicic acid.

Table A1. Phytoplankton Abundance at DCM by Station

Observer ID	Station	Station Name	Seamount Category	Total Counted	# Dino	% Dino	# Bacillario	% Bacillario	# Radio	% Radio	# Cilio	% Cilio	# Hapto	% Hapto
A	e1	esme upstream	upstream, active	317	50	15.8	88	27.8	166	52.4	19	6	0	0
A	e2	esme summit	summit, active	319	39	12.2	137	42.9	133	41.7	10	3.1	0	0
A	n1	nw rota upstream	upstream, active	230	20	9.7	63	30.4	137	66.2	10	4.8	0	0
A	n4	nw rota summit	summit, active	309	15	4.9	71	23	228	73.8	2	0.6	0	0
A	o1	offshore	offshore	347	58	16.7	117	33.7	161	46.4	10	2.9	0	0
A	o2	offshore	offshore	304	17	5.6	95	31.3	180	59.2	12	3.9	0	0
A	t1	tracey upstream	upstream, inactive	305	45	14.8	81	26.6	166	54.4	13	4.3	0	0
A	t2	tracey summit	summit, inactive	313	32	10.2	78	24.9	149	47.6	15	4.8	39	12.5
B	e1	esme upstream	upstream, active	120	21	17.5	51	42.5	25	20.8	13	10.8	1	0.8
B	e2	esme summit	summit, active	211	18	8.5	67	31.8	54	25.6	26	12.3	29	13.7
B	n4	nw rota summit	summit, active	87	14	16.1	42	48.3	19	21.8	5	5.7	6	6.9

610

Table A2. Bray-Curtis Dissimilarity Matrix of Relative Abundances of Major Phytoplankton Taxa at DCM

Station	e1	e2	n1	n4	o1	o2	t1	t2
e1	0	0.159	0.168	0.205	0.076	0.097	0.029	0.138
e2	0.159	0	0.177	0.304	0.101	0.181	0.157	0.199
n1	0.168	0.177	0	0.205	0.201	0.15	0.14	0.153
n4	0.205	0.304	0.205	0	0.248	0.135	0.182	0.246
o1	0.076	0.101	0.201	0.248	0	0.129	0.088	0.184
o2	0.097	0.181	0.15	0.135	0.129	0	0.094	0.17
t1	0.029	0.157	0.14	0.182	0.088	0.094	0	0.12
t2	0.138	0.199	0.153	0.246	0.184	0.17	0.12	0

611

Table A3. Agreement Data for Taxon ID Between Observers

		% Abundance of Major Taxa by Observer					Abundance Rank (1 = Most, 5 = Least)				
Observer	Station	Dino	Bacillario	Radio	Cilio	Hapto	Rank 1	Rank 2	Rank 3	Rank 4	Rank 5
A	e1	15.5	27.2	51.4	5.9	0	Radio	Bacillario	Dino	Cilio	Hapto
B	e1	18.9	45.9	22.5	11.7	0.9	Bacillario	Radio	Dino	Cilio	Hapto
B-A	**e1**	**3.4**	**18.7**	**22.5**	**5.8**	**0.9**					
A	e2	12.2	42.9	41.7	3.1	0	Bacillario	Radio	Dino	Cilio	Hapto
B	e2	9.3	34.5	27.8	13.4	14.9	Bacillario	Radio	Cilio	Dino	Hapto
B-A	**e2**	**-2.9**	**-8.4**	**-13.9**	**10.3**	**14.9**					
A	n4	4.7	22.5	72.2	0.6	0	Radio	Bacillario	Dino	Cilio	Hapto
B	n4	16.3	48.8	22.1	5.8	7	Bacillario	Radio	Dino	Cilio	Hapto
B-A	n4	11.6	26.3	-50.1	5.2	7					
Mean B-A	**e1, e2, n4**	**4**	**12.2**	**-13.8**	**7.1**	**7.6**					

612

Table A4. Bray-Curtis Dissimilarity Between Observer A and B

Station	Name	Bray-Curtis Dissimilarity
e1	Esmeralda Upstream	0.4931
e2	Esmeralda Summit	0.4191
n4	NW Rota Summit	0.6169
e1, e2, n4	**Mean**	**0.5097**

613

614 **References**

615 Baker, E. T., Embley, R. W., Walker, S. L., Resing, J. A., Lupton, J. E., Nakamura, K., de

616 Ronde, C. E. J., & Massoth, G. J. (2008). Hydrothermal activity and volcano distribution

along the Mariana arc. *Journal of Geophysical Research: Solid Earth*, *113*(B8). https://doi.org/10.1029/2007JB005423

Browning, T. J., Achterberg, E. P., Rapp, I., Engel, A., Bertrand, E. M., Tagliabue, A., & Moore, C. M. (2017). Nutrient co-limitation at the boundary of an oceanic gyre. *Nature*, *551*(7679), 242–246. https://doi.org/10.1038/nature24063

Brzezinski, M. A. (1985). THE Si:C:N RATIO OF MARINE DIATOMS: INTERSPECIFIC VARIABILITY AND THE EFFECT OF SOME ENVIRONMENTAL VARIABLES. *Journal of Phycology*, *21*(3), 347–357. https://doi.org/10.1111/j.0022-3646.1985.00347.x

Brzezinski, M. A., Dickson, M.-L., Nelson, D. M., & Sambrotto, R. (2003). Ratios of Si, C and N uptake by microplankton in the Southern Ocean. *Deep Sea Research Part II: Topical Studies in Oceanography, US Southern Ocean JGOFS Program (AESOPS): Part III*, *50*(3), 619–633. https://doi.org/10.1016/S0967-0645(02)00587-8

Comeau, L. A., Vézina, A. F., Bourgeois, M., & Juniper, S. K. (1995). Relationship between phytoplankton production and the physical structure of the water column near Cobb Seamount, northeast Pacific. *Deep Sea Research Part I: Oceanographic Research Papers*, *42*(6), 993–1005. https://doi.org/10.1016/0967-0637(95)00050-G

Clark, M. R., Rowden, A. A., Schlacher, T., Williams, A., Consalvey, M., Stocks, K. I., Rogers, A. D., O'Hara, T. D., White, M., Shank, T. M., & Hall-Spencer, J. M. (2010). The Ecology of Seamounts: Structure, Function, and Human Impacts. *Annual Review of Marine Science*, *2*(Volume 2, 2010), 253–278. https://doi.org/10.1146/annurev-marine-120308-081109

Dai, S., Zhao, Y., Li, X., Wang, Z., Zhu, M., Liang, J., Liu, H., & Sun, X. (2022). Seamount effect on phytoplankton biomass and community above a deep seamount in the tropical

western Pacific. *Marine Pollution Bulletin*, *175*, 113354. https://doi.org/10.1016/j.marpolbul.2022.113354 (a)

Dai, S., Zhao, Y., Li, X., Wang, Z., Zhu, M., Liang, J., Liu, H., Tian, Z., & Sun, X. (2020). The seamount effect on phytoplankton in the tropical western Pacific. *Marine Environmental Research*, *162*, 105094. https://doi.org/10.1016/j.marenvres.2020.105094 (b)

Fennel, K., & Boss, E. (2003). Subsurface maxima of phytoplankton and chlorophyll: Steady-state solutions from a simple model. *Limnology and Oceanography*. https://doi.org/10.4319/lo.2003.48.4.1521

Fitzsimmons, J. N., Boyle, E. A., & Jenkins, W. J. (2014). Distal transport of dissolved hydrothermal iron in the deep South Pacific Ocean. *Proceedings of the National Academy of Sciences*, *111*(47), 16654–16661. https://doi.org/10.1073/pnas.1418778111

Gordon, L. I., J. C. Jennings Jr, A. A. Ross, and J. M. Krest. "A suggested protocol for continuous flow automated analysis of seawater nutrients in the WOCE hydrographic program and the Joint Global Ocean Fluxes Study." *Grp. Tech Rpt* (1993): 92-1.

Hutchins, D. A., & Bruland, K. W. (1998). Iron-limited diatom growth and Si:N uptake ratios in a coastal upwelling regime. *Nature*, *393*(6685), 561–564. https://doi.org/10.1038/31203

Jin, L., Liu, C., Cao, N., Liao, X., Xue, Y., Bao, R., Fan, L., Zhu, L., Su, Q., Yang, K., Zheng, R., Chang, S., & Liang, M. (2024). Tracking the variability of the western Pacific warm pool heat content over 1980–2020. *Frontiers in Earth Science*, *12*. https://doi.org/10.3389/feart.2024.1377715

Kleint, C., Zitoun, R., Neuholz, R., Walter, M., Schnetger, B., Klose, L., Chiswell, S. M., Middag, R., Laan, P., Sander, S. G., & Koschinsky, A. (2022). Trace Metal Dynamics in

Shallow Hydrothermal Plumes at the Kermadec Arc. *Frontiers in Marine Science*, *8*. https://doi.org/10.3389/fmars.2021.782734

Leach, T. H., Beisner, B. E., Carey, C. C., Pernica, P., Rose, K. C., Huot, Y., Brentrup, J. A., Domaizon, I., Grossart, H.-P., Ibelings, B. W., Jacquet, S., Kelly, P. T., Rusak, J. A., Stockwell, J. D., Straile, D., & Verburg, P. (2018). *Patterns and drivers of deep chlorophyll maxima structure in 100 lakes: The relative importance of light and thermal stratification*. https://doi.org/10.1002/lno.10656

Leitner, A. B., Neuheimer, A. B., & Drazen, J. C. (2020). Evidence for long-term seamount-induced chlorophyll enhancements. *Scientific Reports*, *10*(1), 12729. https://doi.org/10.1038/s41598-020-69564-0

Liao, L., Xu, X.-W., Jiang, X.-W., Wang, C.-S., Zhang, D.-S., Ni, J.-Y., & Wu, M. (2011). Microbial diversity in deep-sea sediment from the cobalt-rich crust deposit region in the Pacific Ocean. *FEMS Microbiology Ecology*, *78*(3), 565–585. https://doi.org/10.1111/j.1574-6941.2011.01186.x

Lin, Y.-S., Lee, J., Lin, L.-H., Fu, K.-H., Chen, C.-T. A., Wang, Y.-H., & Lee, I.-H. (2020). Biogeochemistry and dynamics of particulate organic matter in a shallow-water hydrothermal field (Kueishantao Islet, NE Taiwan). *Marine Geology*, *422*, 106121. https://doi.org/10.1016/j.margeo.2020.106121

Ma, J., Li, X., Song, J., Wen, L., Liang, X., Xu, K., & Dai, J. (2023). Distribution patterns of six metals and their influencing factors in M4 seamount seawater of the Western Pacific. *Marine Pollution Bulletin*, *196*, 115664. https://doi.org/10.1016/j.marpolbul.2023.115664

(a)

683 Martin, A. P., Richards, K. J., Bracco, A., & Provenzale, A. (2002). Patchy productivity in the
684 open ocean. *Global Biogeochemical Cycles*, *16*(2).
685 https://doi.org/10.1029/2001GB001449
686 Eppley, R. W., & Peterson, B. J. (1979). Particulate organic matter flux and planktonic new
687 production in the deep ocean. *Nature*, *282*(5740), 677–680.
688 https://doi.org/10.1038/282677a0
689 White, M., Bashmachnikov, I., Arístegui, J. and Martins, A. (2007). Physical Processes and
690 Seamount Productivity. In Seamounts: Ecology, Fisheries & Conservation (eds T.J. Pitcher,
691 T. Morato, P.J.B. Hart, M.R. Clark, N. Haggan and R.S. Santos). https://doi-
692 org.offcampus.lib.washington.edu/10.1002/9780470691953.ch4.
693 Pichler, T., Veizer, J., & Hall, G. E. M. (1999). The chemical composition of shallow-water
694 hydrothermal fluids in Tutum Bay, Ambitle Island, Papua New Guinea and their effect on
695 ambient seawater. *Marine Chemistry*, *64*(3), 229–252. https://doi.org/10.1016/S0304-
696 4203(98)00076-0
697 Shaked, Y., Twining, B. S., Tagliabue, A., & Maldonado, M. T. (2021). Probing the
698 Bioavailability of Dissolved Iron to Marine Eukaryotic Phytoplankton Using In Situ Single
699 Cell Iron Quotas. *Global Biogeochemical Cycles*, *35*(8), e2021GB006979.
700 https://doi.org/10.1029/2021GB006979
701 Resing, J. A., Lebon, G., Baker, E. T., Lupton, J. E., Embley, R. W., Massoth, G. J., Chadwick,
702 W. W., & De Ronde, C. E. J. (2007). Venting of Acid-Sulfate Fluids in a High-Sulfidation
703 Setting at NW Rota-1 Submarine Volcano on the Mariana Arc. *Economic Geology*, *102*(6),
704 1047–1061. https://doi.org/10.2113/gsecongeo.102.6.1047

Resing, J. A., Baker, E. T., Lupton, J. E., Walker, S. L., Butterfield, D. A., Massoth, G. J., & Nakamura, K. (2009). Chemistry of hydrothermal plumes above submarine volcanoes of the Mariana Arc. *Geochemistry, Geophysics, Geosystems*, *10*(2). https://doi.org/10.1029/2008GC002141

Resing, J. A., Sedwick, P. N., German, C. R., Jenkins, W. J., Moffett, J. W., Sohst, B. M., & Tagliabue, A. (2015). Basin-scale transport of hydrothermal dissolved metals across the South Pacific Ocean. *Nature*, *523*(7559), 200–203. https://doi.org/10.1038/nature14577

Ribalet, F., Berthiaume, C., Hynes, A., Swalwell, J., Carlson, M., Clayton, S., Hennon, G., Poirier, C., Shimabukuro, E., White, A., & Armbrust, E. V. (2019). SeaFlow data v1, high-resolution abundance, size and biomass of small phytoplankton in the North Pacific. *Scientific Data*, *6*, 277. https://doi.org/10.1038/s41597-019-0292-2

Rocke, E., Noyon, M., & Roberts, M. (2020). Picoplankton and nanoplankton composition on and around a seamount, affected by an eddy dipole south of Madagascar. *Deep Sea Research Part II: Topical Studies in Oceanography*, *176*, 104744. https://doi.org/10.1016/j.dsr2.2020.104744

Scofield, A. E., Watkins, J. M., Osantowski, E., & Rudstam, L. G. (2020). Deep chlorophyll maxima across a trophic state gradient: A case study in the Laurentian Great Lakes. *Limnology and Oceanography*, *65*(10), 2460–2484. https://doi.org/10.1002/lno.11464

Stern, R. J., Tamura, Y., Masuda, H., Fryer, P., Martinez, F., Ishizuka, O., & Bloomer, S. H. (2013). How the Mariana Volcanic Arc ends in the south. *Island Arc*, *22*(1), 133–148. https://doi.org/10.1111/iar.12008

Strickland, J.D.H., and T.R. Parsons. 1972. A practical handbook of seawater analysis. Fish. Res. Board Can. Bull. 167, 2nd ed. 310 pp.

728 Sunda, W. (2012). Feedback Interactions between Trace Metal Nutrients and Phytoplankton in
729 the Ocean. *Frontiers in Microbiology*, *3*. https://doi.org/10.3389/fmicb.2012.00204
730 Takeda, S. (1998). Influence of iron availability on nutrient consumption ratio of diatoms in
731 oceanic waters. *Nature*, *393*(6687), 774–777. https://doi.org/10.1038/31674
732 Tett, P., Arístegui, J., Barton, D., Basterretxea, G., De Armas, J. D., Escánez, J. E., León, S. H.,
733 Lorenzo, L. M., & Montero, N. (2002). Steady-state DCM dynamics in Canaries waters.
734 *Deep Sea Research Part II: Topical Studies in Oceanography, CANIGO I*, *49*(17), 3543–
735 3559. https://doi.org/10.1016/S0967-0645(02)00097-8
736 Toole, J. M., Schmitt, R. W., Polzin, K. L., & Kunze, E. (1997). Near-boundary mixing above
737 the flanks of a midlatitude seamount. *Journal of Geophysical Research: Oceans*, *102*(C1),
738 947–959. https://doi.org/10.1029/96JC03160
739 Twining, B. S., & Baines, S. B. (2013). The Trace Metal Composition of Marine Phytoplankton.
740 *Annual Review of Marine Science*, *5*(Volume 5, 2013), 191–215.
741 https://doi.org/10.1146/annurev-marine-121211-172322
742 Yan, W., Chen, Z., Zhang, L., Wang, F., Zhang, G., & Sun, J. (2023). Nanophytoplankton and
743 microphytoplankton in the western tropical Pacific Ocean: Its community structure, cell size
744 and carbon biomass. *Frontiers in Marine Science*, *10*.
745 https://doi.org/10.3389/fmars.2023.1147271